Fractional Quantum Anomalous Hall Effect

Ting Cao,[1] Liang Fu,[2] Long Ju,[2] Di Xiao,[1,3] and Xiaodong Xu[3,1]

[1]Department of Materials Science and Engineering, University of Washington, Seattle, WA, USA
[2]Department of Physics, Massachusetts Institute of Technology, Cambridge, MA, USA
[3]Department of Physics, University of Washington, Seattle, WA, USA

Xxxx. Xxx. Xxx. Xxx. YYYY. AA:1–25

https://doi.org/10.1146/((please add article doi))

Keywords

quantum Hall effect, zero magnetic field, topology, twisted $MoTe_2$ bilayer, rhombohedral-stacked multilayer graphene

Abstract

The realization of fractional quantum anomalous Hall effect (FQAHE) in zero-field fractional Chern insulator is a new advancement in condensed matter physics, resulted from the interplay between strong correlations, topology, and spontaneous time-reversal symmetry breaking in lattice systems. In this review, we highlight the experimental and theoretical progress toward achieving FQAHE in two material platforms: twisted bilayer $MoTe_2$ and rhombohedral-stacked multilayer graphene. These systems host narrow topological bands with nontrivial Chern numbers, enabling interaction-driven fractionalized states analogous to the fractional quantum Hall effect, but without external magnetic fields. We discuss how spontaneous ferromagnetism, moiré lattice reconstruction, and band topological effects underpin the emergence of FQAHE in twisted $MoTe_2$. We will describe experimental discoveries of zero-field fractional Chern insulators in both transport and optical experiments, as well as signatures of composite Fermi liquids and higher-energy Chern band which may shed light on engieering non-Abelian states. In rhombohedral graphene/hBN moiré superlattices, we review the recent observations of fractionally quantized Hall resistance, connections between FQAHE and extended quantum anomalous Hall phases, and the coexistence of superconductivity and FQAHE. These discoveries not only deepen our understanding of strongly correlated topological matter but also open new frontiers for exploring non-Abelian anyons, fault-tolerant quantum computation, and topological opto-spintronics free of magnetic fields.

Contents

1. INTRODUCTION

A vibrant frontier in modern condensed matter physics is the study of topological quantum many-body systems, where the interplay between topology and electron-electron interactions gives rise to exotic quantum phases of matter. A seminal example is the integer quantum Hall effect (IQHE) discovered in 1980 (1). In a two-dimensional electron gas subjected to a strong perpendicular magnetic field, the formation of Landau levels leads to a remarkable quantization of the Hall resistance (R_{xy}) in integer multiples of $\frac{h}{e^2}$, accompanied by a vanishing longitudinal resistance (R_{xx}). Two years later, similar quantization of R_{xy} and suppression of R_{xx} were observed at fractional fillings ($\nu = \frac{1}{3}$) of the lowest Landau level in high-mobility GaAs samples (2). This phenomenon, known as the fractional quantum Hall effect (FQHE), arises from electron-electron interactions in partially filled Landau levels and represents a class of electronic phases that lie beyond the conventional Landau symmetry-breaking paradigm (3). Instead, these phases are characterized by the emergence of fractional quasiparticle and topological order. Beyond their fundamental importance, insights from the FQHE and related systems have profoundly influenced the development of fault-tolerant topological quantum computation, leveraging features such as anyonic excitations with non-Abelian statistics (4, 5, 6, 7, 8, 9, 10, 11, 12, 13, 14, 15, 16, 17, 18). The quantized Hall conductance in both the IQHE and the FQHE has been identified as a topological invariant known as the Chern number (19, 20), which now underpins the characterization of Chern insulators. Notably, the Chern number of the many-body ground states is universally defined for all gapped quantum states in two dimensions, and a nonzero Chern number does not require the presence of a magnetic field (20), suggesting that both the IQHE and the FQHE may be realized in systems without an external magnetic field.

The idea of realizing the IQHE without Landau levels has been extensively explored and experimentally achieved. A groundbreaking step was Haldane's proposal of a model on the honeycomb lattice that exhibits the IQHE in the absence of an external magnetic field (21). In this model, complex next-nearest-neighbor hopping breaks time-reversal symmetry, leading to a quantized Hall response without net magnetic flux. Haldane's model describes spinless fermions and serves as a foundational theoretical construct. Building on this concept, Kane and Mele introduced the quantum spin Hall insulator by incorporating spin-orbit coupling into a graphene-based model (22). This system, which can be viewed as two time-reversed copies of the Haldane model corresponding to opposite spin sectors, preserves time-reversal symmetry and exhibits a topologically nontrivial insulating phase. The quantum spin Hall effect was subsequently observed in HgTe quantum wells

(23, 24), providing the first experimental realization of a two-dimensional topological insulator. Three-dimensional topological insulators provide a path to achieving the IQHE at zero magnetic field through time-reversal symmetry breaking and gap opening at the surface Dirac point (25, 26). This phenomenon, known as the quantum anomalous Hall effect (QAHE), was experimentally realized in 2013 in magnetically doped topological insulator thin films (27).

Unlike the IQHE, which can be understood within a single-particle framework, the FQHE fundamentally relies on strong electron-electron interactions (28). Although the formulation of the many-body Chern number does not need a magnetic field (20), it remained unclear whether the FQHE could be realized without an external magnetic field. Initial theoretical efforts investigated this possibility in various contexts, including spin systems (29), periodic lattice potentials (30), and synthetic optical lattices (31, 32, 33, 34, 35). A major breakthrough came in 2011, when several theoretical works firmly established the possibility of a zero-field FQHE, also referred to as the fractional quantum anomalous Hall effect (FQAHE). Several lattice models were proposed to realize a flat Chern band—a Bloch band with flat dispersion and nonzero Chern number (36, 37, 38), and the existence of the FQHE was firmly established through exact diagonalization studies (38, 39, 40). The resulting phase of matter is named as fractional Chern insulator (FCI) (36, 37, 38, 39, 40, 41). Most of these early models (36, 37, 38, 39, 40) focused on spinless fermions, while Ref. (41) extended the analysis to spinful models and proposed the (111) bilayers of transition metal oxides as a viable material platform. Despite their differences, a common theme has emerged: the realization of the FQAHE hinges on engineering a flat Chern band, which simultaneously provides the three essential ingredients—nontrivial topology, strong electronic interactions, and suppressed kinetic energy.

Despite these early theoretical advances, the search for a material realization of the FQAHE continues. The emergence of moiré superlattices in layered two-dimensional materials (42, 43, 44) has opened up a versatile platform for engineering flat electronic bands (45, 46, 47, 48). A prominent example is the discovery of unconventional superconductivity in magic-angle twisted bilayer graphene (MATBG), which highlights the potential of moiré systems to host novel correlated phases (48). Beyond superconductivity, these systems have also revealed emergent phenomena such as orbital magnetism and the QAHE, particularly when MATBG is aligned with a hexagonal boron nitride (hBN) substrate (49, 50). These indicates that not only the moiré bands can be made flat, they can be topologically nontrivial as well. When subjected to a magnetic field, Landau fan diagram measurements revealed fractional slopes at fractional fillings of the moiré unit cell, indicating the presence of interaction-driven topological states. Analysis based on the Streda formula has identified field-induced FCI states in bilayer graphene/hBN moiré systems above 30 T (51) and in MATBG above 5 T (52). Together, these results underscore the promise of moiré flat Chern bands as a viable route toward realizing the FQAHE.

In 2023, the long-sought FQAHE — fractional quantization of Hall resistance at zero magnetic field — was experimentally realized in two different material systems: twisted $MoTe_2$ bilayer (53) and rhombohedral pentalayer graphene aligned with hBN (54). In the following, we review their respective material properties, outline the experimental phenomenology of FQAHE, and discuss future research directions.

2. Moiré bilayer $MoTe_2$

2.1. Modeling

***Moiré Hamiltonian of R-stacked homobilayer*:** The pioneering theory work in Ref. (55) reveals a time-reversed pair of flat Chern bands and quantum spin Hall insulator in twisted $MoTe_2$ bilayer. The topology arises from the layer pseudospin skyrmions (55), which leads to spatially dependent Berry curvature and thus effective magnetic fields (56, 57). Below, we will describe them in detail.

In twisted bilayer TMD, the stacking order—either R-type (i.e., near 0° twist angle) or H-type (i.e., near 60° twist angle)(58, 59)—plays a crucial role in determining the nature of interlayer interactions and the resulting electronic structures(60, 61). For frontier moiré valence bands, the interlayer electronic coupling depends globally on the spin configurations, as dictated by the spin-valley locking, and locally on interlayer stacking configuration. In R-stacked bilayers, the interlayer hopping is generally allowed between the like-spin bands near VBM, while in H-stacked bilayers, such hopping is suppressed due to spin mismatches between unlike-spin bands at VBM. We therefore focus on the R-stacked twisted bilayer. Within the continuum model, the effective Hamiltonian for the K-valley electrons is given by (55)

$$\mathcal{H}_K^{\uparrow} = \begin{pmatrix} -\frac{\hbar^2(\boldsymbol{k}-\boldsymbol{K}_b)^2}{2m^*} + \Delta_b(\boldsymbol{r}) & \Delta_T(\boldsymbol{r}) \\ \Delta_T^{\dagger}(\boldsymbol{r}) & -\frac{\hbar^2(\boldsymbol{k}-\boldsymbol{K}_t)^2}{2m^*} + \Delta_t(\boldsymbol{r}) \end{pmatrix}, \qquad 1.$$

where $\Delta_{b/t}(\boldsymbol{r})$ and $\Delta_T(\boldsymbol{r})$ are the intra- and inter-layer moiré potential, respectively. Due to the spin-valley coupling, the band edge at each valley is spin split, and opposite valleys carry opposite spins as required by time-reversal symmetry (62, 63). The continuum Hamiltonian for the K' valley spin-down electrons can be obtained by applying time-reversal symmetry to $\mathcal{H}_K^{\uparrow}$, resulting in moiré bands with opposite Chern numbers. The moiré potential can be represented as an effective layer pseudospin magnetic field $\boldsymbol{\Delta}(\boldsymbol{r}) = (\mathrm{Re}\,\Delta_T, -\mathrm{Im}\,\Delta_T, \frac{\Delta_b-\Delta_t}{2})$. It has been shown that $\boldsymbol{\Delta}(\boldsymbol{r})$ gives rise to layer-pseudospin skyrmion textures in real space (55), which describes the relative contribution of each layer to the local electronic wavefunction (**Fig. 1*a***).

As a result, the holes in top moiré valence bands experience an effective magnetic field (56, 57), which could be mapped to an effective spin-orbit coupling term acting among localized orbitals, realizing the Kane-Mele quantum spin-Hall model at small twist angles (55). From the local stacking approximations, these frontier orbitals have been identified to localize at two high-symmetry regions (MX and XM) in a single moiré supercell. The MX and XM orbitals are connected by an in-plane C_2 symmetry, and form the two sublattices of a honeycomb structure. Thus, the R-stacked bilayer provides a natural platform for exploring both real-space skyrmion textures and momentum-space topological phases, making it a promising candidate for studying coupled topological and correlated phenomena in the case of strong electron-electron interactions.

One route towards enhanced many-electron interaction is to engineer flat band that quenches the kinetic energy of electrons (46). Of particular interest is interaction-induced topological phases at partial filling of the spinful topological flat bands in twisted bilayer TMD. Based on continuum model (55) and first-principles moiré band structure calculation, it was shown that the flat Chern bands could have relatively uniform Berry curvature, suggesting a resemblance with the lowest Landau level that is conducive to FQAHE (64). Exact diagonalization studies on twisted bilayer $MoTe_2$ (65) and WSe_2 (66) further show that Coulomb interaction can induce spontaneously and fully spin/valley polarized state at

$\nu \leq 1$ (ν is the number of holes in moiré unit cell), and in this setting, FQAHE can emerge at fractional fillings of the flat Chern band of a given valley, leading to FCI with spontaneous ferromagnetism. Building on the foundational work (55), these early theoretical studies (64, 65, 66) suggest a rich phase diagram of interaction-induced phases in twisted bilayer TMD, including QAH and FQAH states as well as other correlated insulating and metallic states to be discussed later.

***Moiré lattice reconstruction and flat Chern bands*:** In moiré superlattices, the low-energy band dispersion is determined by the periodic moiré potential that arises from the interplay of lattice reconstruction, interlayer coupling, and various electrostatic interactions. In particular, for R-stacked twisted bilayer TMD and boron nitride, the absence of inversion symmetry within each layer and the in-plane mirror symmetry between adjacent layers allows finite piezoelectric and ferroelectric polarizations, respectively (67, 68). Compared with twisted bilayer graphene, this polarization results in additional contribution to the moiré Hamiltonian (i.e., an out-of-plane effective magnetic field acting on layer pseudospin) entirely due to reconstruction (69, 70).

Furthermore, the moiré lattice reconstruction is twist-angle dependent, which is negligible at large twist angle, but gradually enhances until forming large domains of high-symmetry, low-energy stacking configurations (i.e., XM and MX) (**Fig. 1*b***). During this process, the competition between piezoelectric and out-of-plane ferroelectric polarization leads to a polarization reversal at these high-symmetry positions (71). This causes a change in sign of the effective magnetic field and reversal in the real-space skyrmion number and, consequently, a change in the Chern number of the topmost moiré valence band observed in $tMoTe_2$ at about 3° to 4° and $tWSe_2$ at about 1° (72, 53, 73, 74).

The complex reconstruction poises significant theoretical and computational challenges. Machine-learning assisted first-principles calculations have been employed to overcome the scaling in computational cost ($O(N^3)$ in plane-wave density functional theory calculations with N corresponding to the size of moiré cell). Machine-learning force fields for $MoTe_2$ and WSe_2 have been constructed using training data from larger twist angle moiré cell or various bilayer unit-cell configurations (71, 75, 76). The trained force field can be used to predict reconstruction patterns at smaller twist angle moiré cells.

The unique reconstruction of the moiré lattice also influences band flatness, resulting in a flat Chern band at twist angles near 3° in $tMoTe_2$ (**Fig. 1*c***) (77, 71, 75, 78). The flat Chern band provide a platform for exploring exotic quantum phases, including zero-field FCIs and higher Landau-level analogs in the absence of a magnetic field (**Fig. 1*d***), as we will discuss next. The ability to engineer such bands via lattice relaxation and polarization effects also provide guidance for designing intertwined topological and correlated states in other moiré platforms.

***FQAHE at fractional filling*:** In twisted bilayer $MoTe_2$, doping the flat band can result in a ferromagnetic ground state due to interaction-driven spontaneous valley polarization (see experimental section below). At integer fillings, twisted bilayer TMDs have been predicted to stabilize as a Chern insulator with quantized anomalous Hall conductance, accompanied by spontaneous time-reversal symmetry breaking (55, 65, 64).

At fractional fillings, the interplay between band topology and strong electron-electron interactions gives rise to a rich phase diagram, including competing states such as ferromagnetic metals (65, 66), generalized Wigner crystals (66), and zero-field FCIs (or FQAHE states) (65, 66, 78, 79, 80, 81). Exact diagonalization studies on first-principles-derived Hamiltonians for $tMoTe_2$ have revealed robust zero-field FCI states near $\nu = -2/3$ for rel-

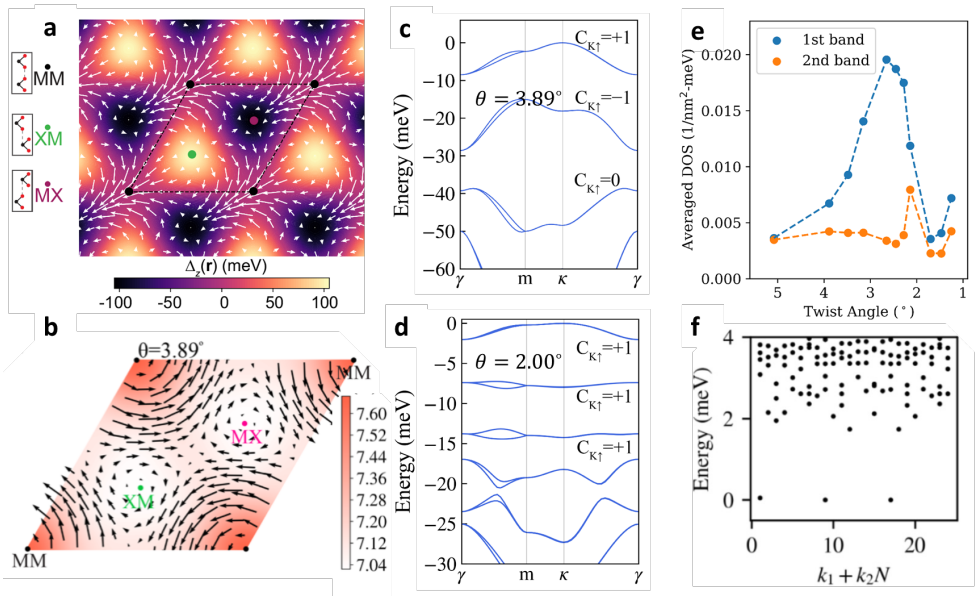

Figure 1

Theory of fractional Chern insulators in twisted bilayer $MoTe_2$ ($tMoTe_2$). (*a*) Layer Pseudospin textures in $tMoTe_2$. MM/XM/MX denotes the stacking where the metal/chalcogen/metal atoms of the top layer are directly above the metal/metal/chalcogen atoms of the bottom layer, respectively. (*b*) In plane atomic displacement (arrows) and interlayer distance (color) in a moiré unit cell due to reconstruction (arrows). The maximal in plane atomic displacement is 0.32 Å. (*c, d*) Moiré mini band structures for K valley calculated from density functional theory at 3.89° and 2.00°, respectively. Chern numbers for the three topmost bands are labeled. (*e*) Calculated averaged density of states, defined as the number of electronic states per valley within the energy window of the first and second moiré band over a unit area, as a function of the twist angle. (*f*) The many-body spectrum, calculated by exact diagonalization in 3.89° $tMoTe_2$, as a function of total crystalline momentum for full valley polarization at $\nu = -2/3$.

atively large twist angles around 3° to 4° (77, 75, 78), coinciding with the experimentally observation that we will discuss later (**Fig. 1*f***).

The stability of FCI states critically depends on the flatness and Chern number of the underlying bands, as well as the band mixing effects (82, 75, 83). First-principles calculations incorporating lattice reconstruction have shown that twist-angle-dependent moiré potential variations enhance band flatness and uniformity of Berry curvatures, promoting FCI formation under near-ideal conditions at optimal angles ($\sim 3.5°$)(77). Numerical studies using exact diagonalization further confirm that these bands support FCI states at $\nu = -2/3$ with significant energy gaps, while $\nu = -3/5$ states remain accessible with increasing interaction strength (77, 84).

***Composite Fermi liquid*:** At half-filling ($\nu = -1/2$) of the topological valence band in $tMoTe_2$, a unique phase emerges: the composite Fermi liquid (CFL). CFL is a non-Fermi liquid formed by composite fermions, originally discover in 2D electron gas systems under strong magnetic fields. Despite the presence of strong magnetic fields, the effective magnetic field experienced by the composite fermions vanishes at exactly half filling of the LLL. Unlike conventional Fermi liquids, the CFL consists of charge-neutral composite fermions formed

by binding two flux quanta to electrons. This phase exhibits metallic behavior but lacks Landau quasiparticles.

Numerical simulations, including exact diagonalization and density matrix renormalization group studies, have provided robust evidence for the CFL in twisted $MoTe_2$ at zero magnetic field (85, 86, 87). These studies reveal that the many-body spectrum at half-filling exhibits momentum-space features consistent with a composite Fermi sea. Remarkably, these signatures align closely with those observed in the half-filled Landau level under strong magnetic fields, but here they arise purely from the intrinsic properties of the Chern band.

Similar to the presence of FQAHE at $\nu = -2/3$ filling, the formation of the CFL at half filling is facilitated by several factors unique to $tMoTe_2$. The small bandwidth of the nearly flat topological bands suppresses kinetic energy, allowing electron-electron interactions to dominate as we discussed in previous sections. Additionally, the Chern band's quantum geometry, characterized by near-ideal Berry curvature and Fubini-Study metric, promotes the stability of the CFL. These features enable the mapping of the half-filled Chern band to a framework analogous to the half-filled LLL, where composite fermion theory has been extensively developed.

Non-Abelian physics*:** A key discovery from the first-principles calculations is that the low-energy moiré electronic structures of $tMoTe_2$ carry multiple isolated flat minibands of $C = 1$, with approximately equal energy spacing at close to 2° twist angle (**Fig. 1*d). This suggest that the analogs to Landau levels exist even beyond the lowest moiré band. Strikingly, the second band can exhibit essential quantum geometric signatures that closely resemble those of the first excited Landau level (1LL), including a large, nearly uniform Berry curvature and trace condition of the Fubini-Study metric.

Through exact diagonalization calculations based on continuum models or Wannier-function based approaches, $tMoTe_2$ have been demonstrated to become a non-Abelian even-denominator FCI at a filling factor of $\nu = -3/2$ (88, 89, 90, 91, 92). These studies, performed on a torus geometry, unveil a many-body ground state with a sixfold near-degeneracy for even total particle number in the half-filled second moiré band, and a twofold near-degeneracy for odd particle numbers. The ground-state degeneracy obtained in the calculated many-body spectrum is consistent with the nature of Pfaffian or anti-Pfaffian states.

The significance of these predictions is twofold. First, they show that non-Abelian FQAH states, which were previously thought to require a half-filled 1LL under high magnetic fields, can be realized in a lattice system without any external field in $tMoTe_2$. Second, from a practical standpoint, the ability to engineer such states in moiré materials may permit more accessible platforms for future experiments on non-Abelian anyons and braided excitations, which lie at the heart of topological quantum computing.

2.2. Experiment

***Electrically tunable spontaneous ferromagnetism*:** An indispensable ingredient for the FQAHE is spontaneous time-reversal symmetry breaking, provided by the spontaneous ferromagnetic order. This was initially observed in twisted $MoTe_2$ bilayers (tMoTe2) in rhombohedral stacking with a twist angle between 3° to 4° (93). Later efforts has expanded the range of twist angle to between 2° to 4.2° (94, 95, 96). Using reflective magnetic circular dichroism (RMCD) measurements, ferromagnetism in a large phase space of hole doping and

electric fields were identified (**Fig. 2*a***). The observed ferromagnetism has strong doping-dependent cohesive fields (H_c) and Curie temperature (T_c). At moiré filling factors ν of -1 and $-2/3$, H_c and T_c are about 100 mT and 14 K, and 25 mT and 4.5 K, respectively (93). At fixed doping, an electric field can control the ferromagnetic properties and eventually suppress the ferromagnetism above a critical value. The critical electric fields are doping dependent, peaking at $\nu = -1$ and $-2/3$ (**Fig. 2*b***). Despite that the exact ground state at large electric field remains to be determined, initial measurements found negative Curie-Weiss temperature, suggesting antiferromagnetic interactions (93).

As described in the theory section, at twist angle of 3° and above, the moiré frontier bands arise from orbitals localized at the two energy-degenerate high-symmetry regions (MX and XM) in a moiré unit cell. These moiré localized orbitals from these two sublattices have significant wave-function overlap inside and among adjacent moiré cells. The direct Coulomb exchange interactions between these carriers give rise to the Stoner-type, valley-polarized ferromagnetism upon doping. Since the moiré sublattices form the basis of the layer pseudospin, applying an perpendicular electric field breaks the degeneracy of the moiré orbitals, and thus the layer pseudospin. This effectively changes the superlattice geometry from honeycomb to triangular, responsible for the observed electric field-induced magnetic phase transition from a ferromagnet to a putative antiferromagnet. With full layer polarization, experiments also observed the revival of ferromagnetism as hole doping increases beyond $\nu = -1$. This is due to the competition between on-site Coulomb interaction energy U and charger transfer energy Δ between the layers (**Fig. 2*c***). When $\Delta < U$, the additional holes can redistribute to the opposite layers and mediate the ferromagnetic exchange interactions between the majority holes located in the triangular lattice. There findings suggest that t$MoTe_2$ offers a powerful platform for investigating a variety of magnetic phases with strong tunability (93).

Spectroscopic evidence of zero-field FCI*:** $MoTe_2$ is unique that it is a direct bandgap semiconductor in the bilayer form (93, 97, 98). This is distinct from other isostructural TMD semiconductors (e.g. MoS_2, WSe_2, $MoSe_2$, WS_2) whose bilayers are indirect bandgap. This direct bandgap feature enables strong photoluminescence (PL) from charged valley excitons (i.e., trions) as an effective probe of magnetism and Chern insulator states. Doping-dependent PL was first carried out to establish the formation of correlated insulators at certain moir'e fillings (72). Suppressed trion PL at both integer and fractional filling ν are observed (**Fig. 2*d). Since the the formation of trion requires extra carriers, trion PL intensity suppression implies the formation of correlated insulating states, which gaps the fermi-surface and impedes the trion formation. The combined trion PL and RMCD results established the correlation-induced ferromagnetic insulating states at both integer and fractionally hole filling of the moiré flat bands, candidates of QAH states.

Making good metal contacts to 2D semiconductors is a known challenge in the community. The initial signature of the zero-field FCI states was then achieved by measuring the fan diagram of the ferromagnetic insulating states through trion PL (**Fig. 2*e***) (72). The fan diagram yields the topological invariants associated with the gaped states via the Streda formula $C = \phi_o \frac{\partial n}{\partial B}$. Here, C is the Chern number, n is the carrier density corresponds to the gapped state, and B is the magnetic field. As shown in **Fig. 2*e***, three dispersive features are obtained at filling factor -1, $-2/3$, and $-3/5$. Compared to the Streda formula, these characteristics provide evidence of the QAH states with Chern number -1, $-2/3$, and $-3/5$. By fabricating a sensing layer WSe_2 in proximity to the twisted $MoTe_2$, $-2/3$ zero-field FCI state was later confirmed via measuring the optical reflectance

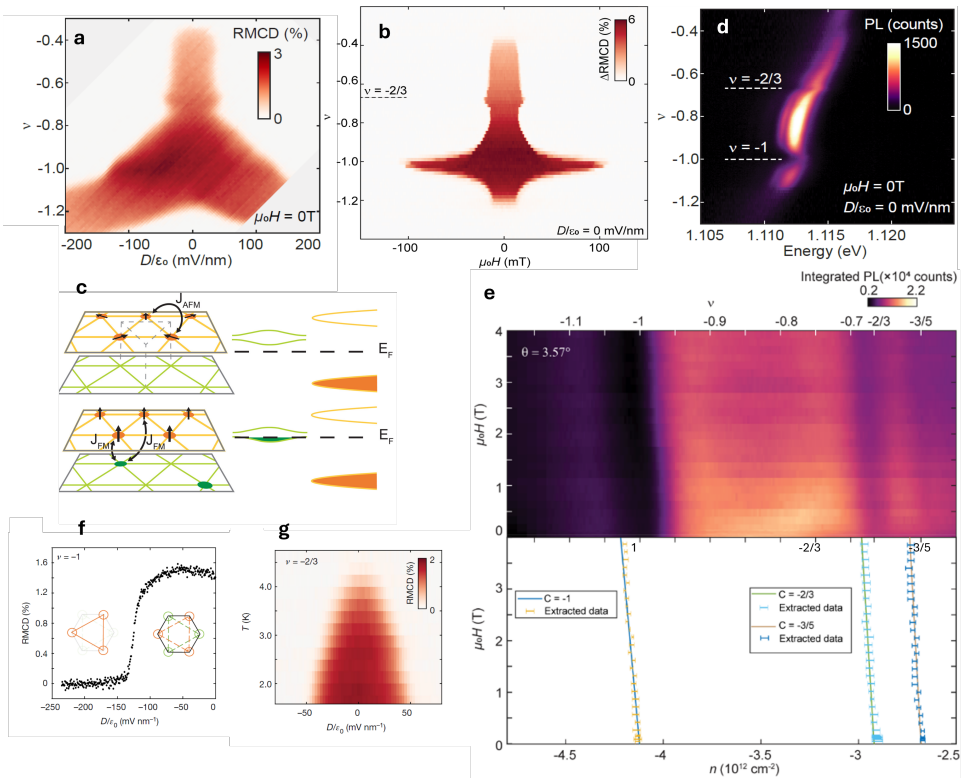

Figure 2

Electrically tunable spontaneous ferromagnetisms and optical sensing of zero-field FCI states. (a) Reflective magnetic circular dichroism (RMCD) signal versus filling factor ν and electric field D of twisted $MoTe_2$ bilayer ($tMoTe_2$). Data is taken at zero magnetic field and temperature of 1.6K. The non-vanishing signal represents the ferromagnetic phase. (b) Difference of RMCD sweeps between forward and backward magnetic fields, ΔRMCD, versus ν and magnetic fields. Clear enhancement of cohesive fields at $\nu = -1$ and $\nu = -2/3$ is observed. (c) Schematic illustration of the interplay between onsite Coulomb interaction and charge transfer energy give rises to the revival of ferromagnetism of a doped Mott insulator at large electric field. See text for details. (d) PL intensity plot verus ν and photon energy, where PL quenching corresponds to the formation of correlated insulating states. (e) The upper panel shows spectrally integrated PL intensity versus magnetic field and ν (or carrier density n), that is, an optical Landau fan diagram. The lower panel shows Wannier diagram corresponding to three Chern insulator states with $C = -1$ $-2/3$ and $-3/5$, respectively. (f) RMCD signal at $\nu = -1$ versus electric field, demonstrating an electric-field-driven magnetic phase transition concurrent with the change in superlattice geometry from honeycomb to triangular (insets). (g) Ferromagnetic phase diagram versus temperature and D at $\nu = -2/3$. Panel c is reproduced from (93). The rest panels are reproduced from (72).

of WSe_2 exciton (73). As described above, the application of the vertical electric field leads to the ferromagnetic phase transition (**Figs. 2*e,f***), which should accompany the QAH phase transition. The observed FM state at $\nu = -2/3$ also has a large T_c **(Fig. 2*f*)** (72). As shown in the following, this leads to zero-field FCI states with large energy gap.

***Transport measurement*:** Establishing zero-field FQHE must require transport measurement of Hall signal (R_{xy}), and direct evidence would be fractionally quantized R_{xy} with

vanishing longitudinal resistance R_{xx} at zero magnetic field. Several schemes have been developed in the community to achieve good metal contacts with TMDs (99, 100). However, these schemes are not feasible to access the phase space with vanishing electric fields across the sample, where layer pseudospin skyrmions form. To address this challenge, Ref. (53) employed local gates for each metal contacts, enabling reasonable contact resistance (tens of KΩ) for twisted $MoTe_2$. **Figs. 3*a,b*** shows the R_{xy} and R_{xx} versus doping and electric fields. The parameter space with suppressed R_{xx} and corresponding enhanced R_{xy} highlights the QAH phases. Integer QAH states are observed near $\nu = -1$, which remains quantized at about 6K, suggesting its large energy gap. Zero-field FCI states are observed at $-2/3$ and $-3/5$ fillings, with the critical temperature of quantization near 2K. The integer and nearly quantized $-2/3$ QAH states are also later confirmed at lower temperature with a different contact design (101). These QAH states can transition into topological trivial insulating states by the application of electric fields, which offers a powerful platform to investigate phase transition between different types of correlated (topological) states. In addition, the ability to switch off the chiral edge current and transition into an insulating state can be potentially useful for the realization of topological transistors.

In the initial observation of FQAHE, although R_{xy} is quantized, R_{xx} remains finite ($\sim 5-10$ KΩ) (**Figs. 3*a,b***). This dissipative behavior is likely due to sample quality, similar to the landmark discovery of FQHE in 1982 (2). Rapid progress has been made in improving $MoTe_2$ crystal. This leads to the observation of the non-dissipation $-2/3$ zero-field FCI state (**Fig. 3*c***) (102, 103). Additional Jain sequence of FCI states are also observed, although R_{xx} remains finite, suggesting a possibility for further improvement in sample quality. Using this high-quality device, the thermal activation gap of the $-2/3$ FCI state was investigated versus magnetic field B (102). Unlike FQHE states with an energy gap increasing as $\sqrt{B}$, and the field-induced FCI where the energy gap increases with B (52, 104), the thermal activation gap of the FCI states drops rapidly as the magnetic field increases and then plateaus at a higher field. This observation is attributed to the two-gap behavior. At zero magnetic field, spin-fluctuation/magnetic domain dominated transport behavior near Curie temperature. As magnetic field increases, the spin fluctuation is suppressed and eventually frozen, giving rise to the intrinsic FCI gap. Note that the energy gap of both integer and fractional QAH states are quite high, which is due to the strong carrier-carrier interactions from close carrier separation on the order of moire wavelength as well as reduced screening effect in the atomically-thin limit.

Scanning probe measurements*:** An intrinsic property of FCI is the bulk-boundary correspondence, i.e., edge conduction with insulating bulk states. This property was investigated by a light-coupled scanning microwave impedance microscopy (MIM) technique (105). An open challenge for scanning probe measurements of local conductance is the screening of the metallic tip by the top gate. This challenge is overcame by utilizing a monolayer WS_2 as a top gate. Monolayer WS_2 is a semiconductor. However, under light illumination, photo-excited carriers in WS_2 is mobile enough to function as a gate while not fully screen the tip. Scanning MIM measurements of the bulk states as a function of doping and electric field resembles the FQAH phase diagram in transport (**Fig. 3*d). At small electric field, there are local conductivity minimum at $\nu = -1$, $-2/3$, and $-3/5$, corresponding to the integer and fractional Chern insulator states. At large electric field, the conductivity minimum is also observed at $\nu = -1$ and $-2/3$, which suggests a correlated insulating state. There is a metallic regime near critical electric fields, which corresponds to the gap closing during the electric field-induced Chern insulator to correlated insulator

phase transition. By scanning the MIM tip across the sample, conductive edge state with insulating bulk is visualized at Chern insulator states (inset, **Fig. 3*d***). Further, the edge states vanishes for the correlated insulator at large electric field at fixed doping (e.g., at $\nu = -2/3$), supporting that the edge conducting channels are due to the formation of FCI states, rather than from charge accumulation at the sample edge.

QAH states and associated magnetic properties have also been probed via a scanning nano-SQUID (106). Scanning nano-SQUID is a sensitive local measurement of stray magnetic fields. The experiment reveals a ferromagnetic phase diagram nearly identical to magnetic circular dichroism measurements. Since the orbital magnetization varies as the chemical potential is swept through the Chern insulator gap, both DC and AC measurements show several Chern insulators (**Fig. 3*e***). Remarkably, the thermal dynamic gap of the $-2/3$ state measured to be about 7 meV. Nano-SQUID spatial map also reveals significnat moiré disorder in the exact device used in the transport measurement (53). However, because of the very large gap of the FCI states, transport measurement can still observe fractionally quantized Hall resistance despite the existence of moir'e disorder.

Signature of CFL state*:** An intriguing observation in the transport measurement of the 3.7° twisted sample is that the anomalous Hall signal R_{xy} is approximately $2h/e^2$ at half filling and varies linearly as ν, suggesting the state is compressible (**Figs. 3*b,c) (53, 102). In the entire regime, R_{xx} is finite (5-10 KΩ). In fact, the behavior of the state resembles that was observed near half-filling of the LLL in a two-dimensional electron gas at high magnetic fields (108). In the latter case, the state was found to be a CFL state (109, 110, 111, 112, 113, 28). Although the evidence so far does not prove a zero-field CFL state, numerical calculations of the exact $MoTe_2$ system demonstrated an CFL state at half filling as we discussed in the theory section (86, 85).

An additional support to the zero-field CFL state is provided by the trion sensing measurement (107). The trion PL intensity and energy do not show, respectively, appreciable suppression and shift near half filling, which is consistent with the compressible nature of the CFL state. By performing helicity resolved measurements, the degree of circular polarization (ρ) is near unity within the ferromagnetic phase at doping without the formation of QAH states. However, at both integer and fractional QAH states, and near $-1/2$ filling, ρ is strongly quenched (**Fig. 3*f***). Temperature dependent measurements shows ρ increases as temperature increases, and approaches unity at a critical temperature where R_{xy} starts to deviate from quantized values, and eventually drops as temperature approaches the Curie temperature. This behavior can be explained by the local charge excitation gap (or pseudo-gap) of the CFL state (114). To form spin-polarized trion, the photo-excited electron-hole pair needs to bound a spin-polarized hole. However, in the CFL state, excite a spin-polarized hole needs to overcome the pseudo-gap of the CFL state (114), which thus suppress ρ. The temperature dependence implies the thermal activation behavior of the CFL state. This interpretation is further supported by the electric field dependence. For the non-(F)QAH state, ρ is near unity at small electric field, and then drops at large electric field where ferromagnetism is quenched. For the (F)QAH states or the putative CFL state, ρ is suppressed at small electric fields, and revives to unity when the electric field is increased to phase transition boundary where the gap is closed, and then drops as ferromagnetism is destroyed at very large electric field. The concurrent RMCD measurements with the presence of excitation laser show that the signal behaves similarly for all fillings, i.e., near plateau at small electric fields and then vanishes at large ones where FM state is gone. This rules out spin depolarization induced by photo-excitation as the explanation. To

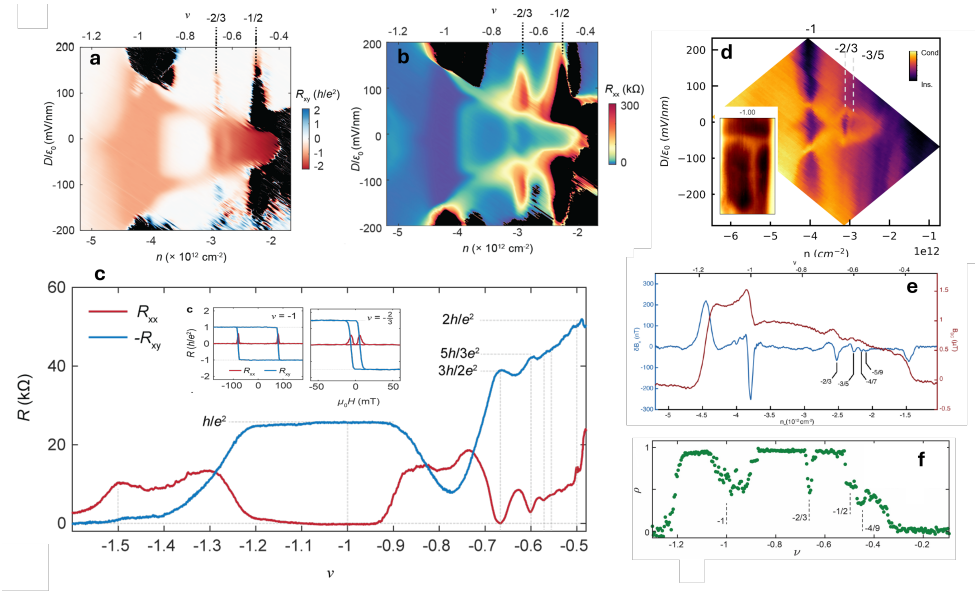

Figure 3

Transport and scanning probe measurements of FQAHE in $tMoTe_2$. (a) Longitudinal (R_{xx}) and (b) Hall (R_{xy}) resistance as a function of electric field D and carrier density n at 100 mK. The data are reproduced from (53). (c) Symmetrized R_{xx} (red) and antisymmetrized $-R_{xy}$ (blue) at $B = \pm 100$ mT versus ν below 30 mK. Jain sequence $-\frac{p}{2p-1}$ ($p = 2, 3, 4, 5$) FCI states are observed. Inset: Measurement of R_{xx} and R_{xy} as a function of magnetic field for the $C = -1$ and $-2/3$ QAH states. Data is reproduced from (102). (d) The MIM-Im signal as a function of displacement field and carrier density at 1.5K. Inset: Spatial map of MIM-Im at the QAH state, showing the conducting edge state with a insulating bulk. Data is reproduced from (105). (e) DC (red) and AC (blue) measurement of local magnetic field by nano-squid versus ν at 1.6 K, which reveals abundant FCI states. Data is reproduced from (106). (f) Degree of circular polarization ρ of trion photoluminescence at 1.6K versus ν. Drops are visible in ρ around $\nu = -1$, $-2/3$ and $-1/2$, as well as an additional dip consistent with the $\nu = -4/9$ Jain state. Data is reproduced from (107).

establish a solid Fermi surface, measurements should be performed as those done in 2DEGs, such as the surface acoustic wave and the anti-dot lattice (111, 112). Another possibility is to use MIM measurement with its capabilities in resolving fermi-wave vector.

Higher-energy Chern bands: So far, the FQAHE phase diagram of first Chern band with partial hole filling behaves like the FQHE one in the LLL. All observed FQAHE states resemble the Jain sequence FQHE states in odd denominators. These states are expected to host Abelian anyons. Certain FQHE states in higher Landau levels, such as 5/2 state (108), are promising candidates to realize non-Abelian anyons (108, 115, 116, 117, 118, 15, 119). Thus, a natural route to create non-Abelian FCI states is to explore higher energy moiré Chern band beyond the first one (89, 88, 90, 91, 120, 92).

Experiments have been carried out to investigate higher energy Chern band. We will separate the discussion into two categories regarding the twist angles. The first group is samples with a twist angle ranging between 2.4° and 4°. Spontaneous ferromagnetism is observed at $\nu = -3$ by RMCD measurements (94). Transport measurements reveal

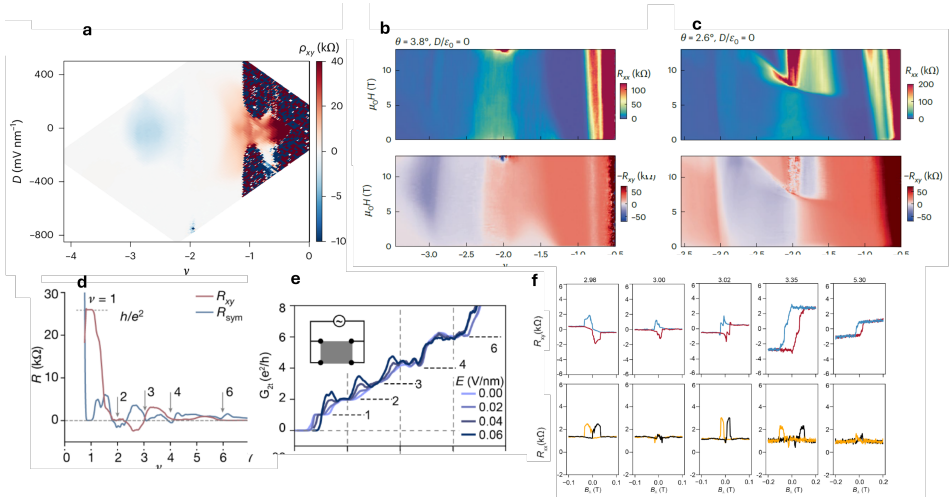

Figure 4

Topology and magnetism of the second flat Chern band. (*a*) Antisymmetrized Hall resistivity at $B = \pm 0.1$ T and 1.6 K versus ν and D for a 3.15° twisted device. The panel is reproduced from (121). (b) Landau fans of symmetrized R_{xx} (top row) and (a) antisymmetrized $-R_{xy}$ (bottom) at T of about 30 mK for a 3.8∘ device. (c) The same as (b) for 2.6° tMoTe2 device. Figures are reproduced from (94). (d) Four-terminal resistance R_{sym} (blue, subtracting an constant resistance) and Hall resistance R_{xy} (red). The dashed lines denote the expected resistance around $\nu = 1$, 2, 3, 4 and 6. (e) Two-terminal conductance versus ν at selected electric fields. Figures are reproduced from (122) (f) Magnetic field dependence of R_{xy} (top) and R_{xx} (bottom) near ν of 3 (hole doping) at 20 mK. Figures are reproduced from (96).

anomalous Hall signal R_{xy}, which is appreciable but smaller than h/e^2 and R_{xx} (94, 121) (**Fig.** 4***a***). At high magnetic field, quantized R_{xy} (h/e^2) and strong R_{xx} dip are observed. Combined with the fan diagram revealing the Streda slope with $|C| = 1$, the state is identified as an incipient Chern insulator state with gap opened by magnetic fields. What is interesting is that the Streda slope, *i.e.* the Chern number, switches sign as a function of twist angle (**Figs.** 3***b,c***). It has an opposite sign compared to the first Chern band for large twist angle, and the same sign at low twist angle. The latter case is further confirmed by the observation of field-induced $|C| = 2$ Chern insulator state near v=-2 (**Fig.** 4***c***). The exact angle where the sign switching happens has not been experimentally determined, but expected to be between 2.6 and 3 degrees, based on both theory (71) and available experimental data(94, 121). So far, no noticeable features at ν = -5/2 have been reported. At 3/2, large R_{xx} with vanishing R_{xy} has been observed either at zero magnetic field for a large twist angle (3.7°) (102) or high magnetic field for small twist angles (2.6° degrees) (94). These observations suggest a topological trivial correlated insulating state at ν =-2/3 within studied twist angle range.

Calculation shows the bandwidth of the second Chern band has a strong dependence on twist angle, and becomes really flat near 2.1 degree (71). Initial transport measurements report zero anomalous Hall conductivity at ν =-3 (**Fig.** 4***d***). Combined with nearly quantized two-terminal conductance (after subtracting a constant background, **Fig.** 4***e***), the results are interpreted as fractional quantum spin Hall (FQSH) effect resulted from a

time-reversal pair of the even-denominator 3/2-FCI (122). In addition, single, double, and triple QSH at ν = 2, 4 and 6 were reported (**Figs.** 4***d,e***). These results generate great interest in the community. Both time-reversal symmetric and broken states have been proposed for the ν = -3 state (120, 88, 123). Soon after, robust ferromagnetism at ν = -3 in 2.1 degree twisted sample was reported by RMCD measurements (95). This shows that the state has broken time reversal symmetry. Recently, the same group, which reported FQSH, performed additional measurements and observed finite R_{xy} at zero magnetic field with a small hystersis loop (**Fig.** 4***f***) (96). Interesting, Rxy vanishes at finite magnetic field. This result is interpreted as time-reversal symmetry broken FQSH. The exact nature of the state remains unknown. Investigations with high-quality devices are needed to rule out trivial causes, such as magnetic domains and moire disorders known to exist in tMoTe2 samples. Other techniques, such as MIM measurements to image the conducting edge with insulating bulk would be necessary to support a QSH edge state (124). Another interesting observation of the initial report of FQSH is a R_{xx} dip with a nearby R_{xy} shoulder between ν of -1 and -2. The state was later interpreted as 3/2 FCI state (96) (**Fig.** 4***d***). Future studies with additional devices and measurements are needed to explore this interesting feature. For instance, a fan diagram is necessary to show whether the R_{xx} dip shifts versus B field, and extract the Chern number via Streda formula analysis. Nevertheless, Chern band beyond the one has already shown glimpse of promise for searching exotic FCI states.

3. Graphene

3.1. Background

***Tunable flat band and Berry curvature*:** As a crystalline form of graphite, rhombohedral stacking (Fig. 5a) is a meta-stable form which has higher energy than the Bernal stacking(125, 126, 127). It features an electrically tunable band gap and Berry curvature(128, 129, 130, 131, 132, 133, 134, 135). Different from $MoTe_2$, the band gap in pristine rhombohedral graphene is zero, while a band gap can be induced by applying a vertical electric field through the top and bottom gates. The essence of the band structure can be understood by a simple tight-binding picture: electrons from the two sublattices within the same layer remain degenerate at zero energy; by hopping to the overlapped sublattice in the next layer, one of the degenerate states are pushed away from zero energy; in the N-layer rhombohedral graphene, only two states at the sublattices located at the outmost layers remain degenerate at zero energy. The two degenerate states are analogs of the dangling bonds in the Su-Shrieffer-Heeger model(136), and they develop into the two lowest-energy bands near the Fermi level. In the pristine form without gating, a band gap can spontaneously open due to the instability a the band-touching point, in the suspended(137, 138, 139, 140, 141) or hBN-encapsulated(142, 143, 144) configurations. By breaking the sublattice degeneracy through a gate-induced vertical displacement field D (145, 146, 147, 148, 142, 149), a band gap can be opened and tuned continuously (Fig. 5b). Subsequently, the density-of-states at the band-edge can be greatly enhanced at optimal gate-displacement field(54), making it a potential playground of electron-correlation effects. In the full tight-binding calculation that includes all the hopping terms, the conduction and valence bands develop an asymmetry and the trigonal warping effect(142). These details will contribute together with the tuning of D to the band dispersion. As the layer number is increased from 1 to 5, the density-of-states increases monotonically near the band edge and drives stronger electron correlation effects.

In the momentum space, the two degenerate valleys K and K' feature opposite Berry curvatures at the same band-edge to conserve the time-reversal-symmetry(150, 151). When the correlation effect is strong enough, the valley (and/or spin) degeneracy can be spontaneously broken due to the exchange interaction similar to that of the Stoner mechanism of ferromagnetic metals(152, 151). Consequently, orbital magnetism and anomalous Hall effect could emerge due to the spontaneous valley polarization. The latter is the key underlying factor for the observation of the FQAHE in experiments on rhombohedral graphene/hBN moiré superlattices.

Moiré superlattice and Chern insulators: When placed on a hexagonal boron nitride (hBN) substrate, the lattice mismatch between rhombohedral graphene and hBN naturally leads to a moiré superlattice(153, 154, 155). The period of this superlattice is about 15 nm at zero twist angle and can be tuned to smaller at non-zero twist angle. The superlattice potential further modifies the band structure of rhombohedral graphene and can induce band gaps at the boundary of the mini-Brillouin Zone(156, 157, 148). Consequently, in the moiré superlattices between hBN and rhombohedral tri- and tetra-layer graphene, Chern insulators and integer quantum anomalous Hall effects have been observed at the hole-doping side(158, 159, 160). The Chern numbers of such states can be as big as 4, larger than in magnetic topological insulators and other moiré superlattice materials(27, 161, 162, 50), but smaller than that observed at the charge-neutrality of rhombohedral pentalayer graphene/WS_2 in the absence of moiré effects(149). These high-Chern-number topological flat bands could be a playground to explore fractional electron states that are beyond what is possible in Landau levels (limited to Chern number 1), but no FCI states have been observed so far.

In general, Chern insulator gap-opening at $\nu = -1$ on the hole-doping side of rhombohedral graphene/hBN moiré superlattice is expected at the single-particle level(158, 157, 163). The Chern number is expected to be the same as the layer number of graphene, although electron interaction effects could modify the Chern number depending on the effective dielectric constant used(158). These properties were not expected for the electron-doping side.

3.2. Experiment

Transport measurement at 300 mK electron temperature: The FQAHE in rhombohedral pentalayer graphene/hBN moiré superlattice was observed directly through transport experiment(54). In the first two devices, a moiré wavelength of 11.5 nm existed between the top-most graphene layer and the top hBN flake (Fig. 5c), corresponding to a twist angle of 0.77°. At the electron-doping side, large anomalous Hall signals was observed at D = +0.8-1 V/nm, where the correspondent electrons in the conduction band are polarized to the layer farthest from the moiré superlattice rather than closest to moiré. Especially, vertical stripes in the n_e - D maps of longitudinal and transverse resistances can be see at integer and fractional moiré filling factors (**Fig.** 5d & e). Quantized $R_{xy} = h/(\nu e^2)$ and corresponding dips in R_{xx} were observed at the moiré superlattice filling factor $\nu = 1$, 2/3, 3/5, 4/7, 4/9, 3/7 and 2/5 (**Fig.** 5f). All fractional states follow the Jain sequence(109) of the fractional quantum Hall effect. When an out-of-plane magnetic field is applied, the signatures of these integer and fractional states show dispersions with slopes that agree with the Streda formula. At half-filling, an anomalous Hall resistance of $2h/e^2$ was observed but without a plateau. The R_{xy} varies linearly with ν in the neighborhood of $\nu = 1/2$. These

observations are aligned with that of the composite fermions in the fractional quantum Hall systems at half-filling of the lowest Landau level(108, 109, 110).

Following the observations made in pentalayer graphene devices, FQAHE was also observed in tetralayer graphene(164) ($\nu = 2/3$ and $3/5$, **Fig.** 5g) and hexalayer graphene(165) ($\nu = 2/3$) through electron transport experiments. These observations indicate that rhombohedral graphene/hBN system is a family of FQAHE materials, and point to the possibility of finding FQAHE in even thicker layers of rhombohedral graphene.

Transport measurement at 30 mK electron temperature: One observation in the first FQAHE experiment in rhombohedral pentalayer graphene/hBN moiré superlattice was the large residue of $R_{xx} = 8$ kOhm at fractional fillings (R_{xx} at $\nu = 1$ was shown to be less than 5 Ohm and limited by experimental noise). This is significantly higher than the values in the state-of-the-art fractional quantum Hall material systems. However, later in a higher quality pentalayer graphene device made by the same group, R_{xx} down to 500 Ohm was observed(164) at an electron temperature estimated to be 30 mK (Fig. 6d). This electron temperature was estimated based on the temperature reading when a superconducting transition happens in a graphene superconductor. At the same time, two more fractional states at $\nu = 5/11$ and $5/9$ were observed. It is therefore reasonable to expect a vanishing R_{xx} of FQAHE with further efforts on improving the device quality.

In addition to the total of 8 FCI states observed at the base electron temperature of 30 mK, three extended regions on the n-D phase diagram exhibit integer quantum anomalous Hall effect(164) at moiré filling factors other than 1 as shown in Fig. 6a & b. These states, named as Extended Quantum Anomalous Hall (EQAH) states, showed nonlinear voltage-current relations in both the longitudinal and transverse directions. The vanishing R_{xx} and quantized R_{xy} both break down at a threshold longitudinal current. This behavior is reminiscent of the de-pinning of Wigner crystals, if one thinks the depinning electric field is in the transverse direction when a current is driven in the longitudinal direction. These EQAH states are interpreted as either similar to the re-entrant quantum Hall effect(166, 167, 168, 169, 170, 171) in which an underlying integer quantum Hall insulator co-exists with a Wigner crystal of holes, or the anomalous Hall crystal state that was proposed recently(172, 173, 174, 175, 176, 177, 178, 179).

We note that the competition between EQAH state and FQAHE at $\nu = 2/3$ is unusual and depends on the sample quality. Pentalayer device D1 and D2 make an ideal pair for comparison: they share the same hBN flakes, the same rhombohedral domain in the graphene flake before cutting, and therefore the same twist angle between graphene and hBN. During the transfer and measurement process, device D1 might have developed more disorders (as evidenced by an R_{xx} minimum of 2 kOhm) than in device D2 (an R_{xx} minimum of 500 Ohm). As a result, the FCI state at $\nu = 2/3$ is replaced by the EQAH state at the base electron temperature of 30 mK in D1, while the same FCI state persisted in D2. Similar re-entrant quantum Hall effect has been observed in GaAs-based two-dimensional electron gas systems, where some weak FQH states are replaced by the integer quantum Hall state at the base temperature. However, the 2/3 FQH state is usually the most robust fractional state against other competing states, while the 2/3 FCI state in the rhombohedral graphene/hBN system seems to lose the competition before other FCI states do. Phenomenologically, we conclude that FCI states are more robust in less disordered devices, similar to the FQH states in GaAs systems. This observation and the temperature dependent evolution of the $v = 2/3$ state agree with recent theories on the competition between FCI and EQAH states.

Superconductivity co-existing with FCIs: Another important observation at lower

electron temperature is a superconducting state, which extends along the boundary of the insulating region near FCI states(164) (**Fig.** 6a). The superconducting transition temperature is about 60 mK. We note that chiral superconductivity has been observed in pentalayer and tetralayer rhombohedral graphene devices in the absence of moiré effects(180). At this moment, it is not clear if the superconductivity observed in moiré devices is chiral superconductivity. Co-existing superconductivity and FCI with similar charge density and displacement field conditions could enable novel gate-defined junction devices for engineering para-fermions(181, 182) for topological quantum computation applications in future.

These experiments revealed several unusual aspects that are obviously different from $MoTe_2$ and the recipe of realizing FQAHE by previous theories(183, 184). Firstly, FQAHE was observed when the electrons in the conduction band are polarized to the opposite layer of the moiré superlattice, which imposes a very weak if not negligible moiré potential to these electrons. Secondly, even if a weak moiré potential is considered, one would not obtain an isolated first moiré band in the single-particle picture as in theoretical models of FCI in twisted $MoTe_2$. Thirdly, the key ingredients that play an important role in FQAHE of the twisted $MoTe_2$, such as strong spin-orbit-coupling and layer pseudospin skyrmions, are absent from the graphene/hBN moiré superlattice. Since the experiment was announced in 2023, a plethora of theoretical works have appeared to discuss these puzzles(185, 186, 187, 188, 173, 177, 189, 179, 190, 191, 174, 192, 178, 193, 194**?** , 195). New concepts such as anomalous Hall crystals were proposed(173, 174, 175, 176, 177, 178, 179, 172), but the underlying mechanism of FQAHE and even the integer QAHE in this material system is still under debate.

Thermodynamic measurements: Complementary to the electron transport measurement that established FQAHE, thermodynamic measurements of the FCI gap have been performed on rhombohedral penta- and tetra-layer graphene/hBN moiré superlattice devices. In a work performed on tetralayer graphene by measuring the capacitance(160), incompressible states were observed at filling factors 2/3 and 1, corresponding to the same FCI states that exhibited FQAHE in transport measurements. These states follow the Streda formula $C = \phi_o \frac{\partial n}{\partial B}$, where C is 2/3 and 1, respectively, similar to the bahavior of R_{xx} minimum under a perpendicular magnetic field in transport measurement. The gap size was extracted to be 24 K and 2.7 K for the integer and fractional states, respectively.

In another capacitance experiment performed on the pentalayer graphene(104) (**Fig. 6e**), the authors focused on the situation when electrons in the conduction band are polarized towards the moiré superlattice and subject to a strong moiré potential. In transport measurement, no signatures of anomalous Hall was found in this situation (corresponding to the opposite displacement field from where FQAHE was observed). However, the compressibility measurement discovered integer and fractional Chern insulator states emerging at as low as 0.2 T (Figs. 6f & g). These states stem from filling factors 1, 2/3 and 1/3 and feature the corresponding Chern numbers of -1, $-2/3$, and $-1/3$, respectively. The phenomena are distinct from those observed on the weak-moiré potential side of displacement field, as the Chern number at the same filling factors are opposite in the strong and weak moiré potential limits. Rhombohedral graphene/hBN moiré superlattices, therefore, host FCI states in two disparate conditions that can be switched in situ by tuning the gate electric field, and provide a unique testbed for any theory on achieving FCI in a general setting.

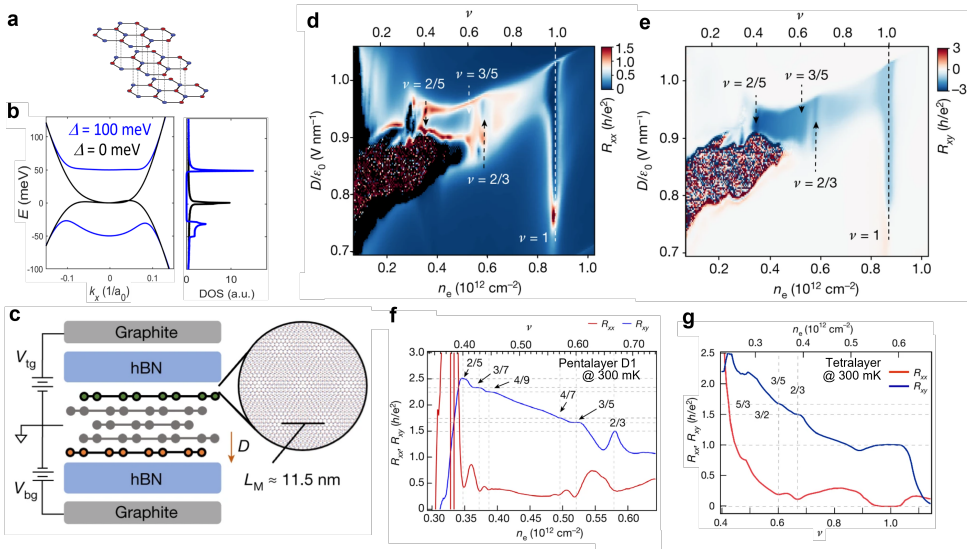

Figure 5

Obeservation of FQAHE in rhombohedral penta- and tetra-layer graphene/hBN moiré superlattices. **a**. Atomic structure of rhombohedral trilayer graphene. **b**. Tight-binding calculation of the band structure and density-of-states (DOS) in rhombohedral pentalayer graphene. Degenrate flat bands exist at interlayer potential $\Delta = 0$ meV, while even more flat band bottom can be induced by $\Delta = 100$ meV. **c**. Device structure of dual-gated rhombohedral pentalayer graphene/hBN moiré superlattice, featuring a moiré wavelength of 11.5 nm between the top-most graphene layer and top hBN flake. **d** & **e**. R_{xx} and R_{xy} as a function of displacement field and charge density, taken at an electron temperature of 300 mK, featuring vertical stripes at integer and fractional moiré filling factors. **f** & **g**. Line-cuts of R_{xx} and R_{xy}, showing quantized plateaus and dips at fractional filling factors of the FQAHE.

4. Summary

The discovery of FQHE about forty years ago transformed our understanding of strongly interacting topological phase of matter, and revealed the existence of exotic quasi-particles - anyons which could have far reaching impact in quantum information science. The realization of the lattice analog of FQHE at zero magnetic field, i.e. FQAHE, in both $tMoTe_2$ and rhombohedral stacked multilayer graphene at elevated temperature provides a laboratory to explore new device schemes and topological states with strong interactions. For instance, the recent discovery of valley-polarized superconductivity in rhombohedral stacked multilayer graphene (196) highlights such opportunities for creation of new strongly-correlated topological states of matter not existing in other systems.

The use of moiré quantum materials offers excellent structural tunability, allowing full exploration of the many-body topological phase diagram by controlling the twist angle, moiré geometry, electric field, and doping. Rich magnetic states, topological states, and potential topological phase transitions can be explored in a controllable fashion. Those point to new directions for both theoretical and experimental investigations. For instance, the semiconducting nature of $tMoTe_2$ offers an opportunity to harness the strong coupling between light, spin, and topology for developing topological opto-spintronics (197). The

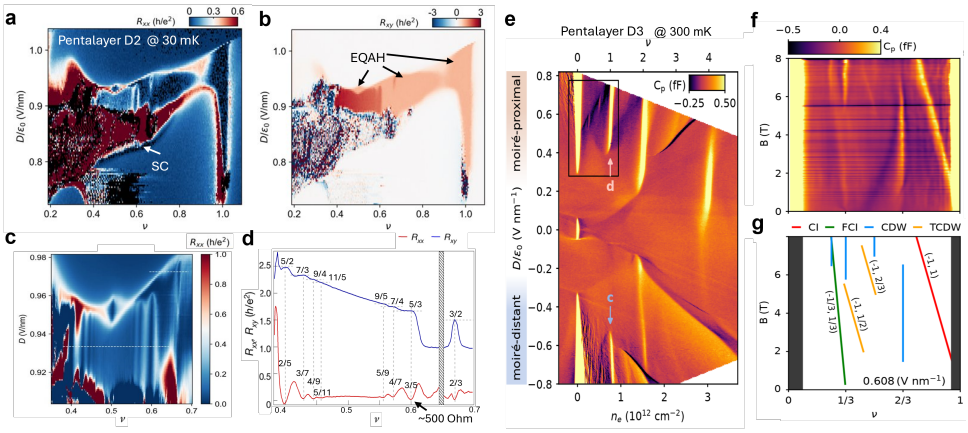

Figure 6

FQAHE, EQAH states and superconductivity at 30 mK electron temperature. a & **b**. R_{xx} and R_{xy} as a function of displacement field and charge density in pentalayer device D2, taken at an electron temperature of 30 mK. New features showing extended region of integer quantum anomalous Hall effect (labeled as 'EQAH') and superconductivity (labeled as 'SC') co-exist with FCI states. **c**. Zoomed-in map of **a**, showing dlear vertical stripes corresponding to 8 FCI states. **d**. Line-cuts of R_{xx} and R_{xy} along the dashed lines in **c**, featuring 8 FCI states with a minimal R_{xx} of 500 Ohm at $v = 3/5$. **e**. Penetration capacitance as a function of density and displacement field at 0 T. Bright features correspond to incompressible states. The box features incompressible states at $v = 1/3$, $2/3$ and 1 at the moiré-proximal side, corresponding to generalized Wigner crystal and correlated insulator states. **f** & **g**. Landau fan diagrams of the penetration capacitance at $D/\epsilon_0 = 0.608$ V/nm, featuring an FCI state emerging from 0.2 T. Additional features include Chern insulator (CI), charge density wave states (CDW), and topological charge density wave states (TCDW).

zero-field and high temperature features of these FCI states also open up measurement opportunities which is otherwise not possible, such as photoemission spectroscopy for visualizing Fermi sea of composite fermions.

An exciting and challenging task is to establish the *anyon* statistics of the zero-field FCI states and search for new states beyond those analogous to Laughlin states in the FQHE. It will be intriguing to engineer high Chern number moiré flat bands, which could potentially host even denominate states, such as 5/2 states. Its counterpart in the FQHE is a candidate of Moore-Read Pfaffian state. The magnetic field free and high temperature nature of these FQAH states make it possible to test proposals for non-abelian anyons, such as Chiral majoran fermion. There are also theoretical proposals for engineering non-Abelian anyons (such as parafermion) by interfacing superconductors with Abelian FQH states. However, the strong magnetic field (> 10 T) required for the formation of FQH states would either destroy superconductivity or generate vortices which prevent the formation of parafermion.

Platform with FQAHE would offer the opportunity to overcome the above challenges, and offer a paradigm shift in researching non-abelian anyons. For instance, the coexistence of superconductivity and FCIs in rhombohedral multilayer graphene could enable the creation of atomic seamless Josephson junctions in single materials. It may eventually allow the test the braiding statistics of non-Abelian anyons in natural materials. Non-Abelian anyons have a degenerate ground state manifold. Adiabatically interchanging the position

of quasiparticles causes the degenerate ground state to undergo a nontrivial unitary transformation. Such unitary operations are only determined by the topology of the interchange, and may be used to construct a universal set of quantum gates. This topologically protected architecture is insensitive to local perturbations and noise, which would solve the primary roadblock – errors and quantum decoherence – to achieving the grand goal of scalable and useful quantum computation.

DISCLOSURE STATEMENT

The authors are not aware of any affiliations, memberships, funding, or financial holdings that might be perceived as affecting the objectivity of this review.

ACKNOWLEDGMENTS

D.X. and X.X. acknowledges the support from the U.S. DOE, BES, under the award DE-SC0012509 and Center on Programmable Quantum Materials, an Energy Frontier Research Center funded by DOE BES under award DE-SC0019443. X.X. also acknowledges the Vannevar Bush Faculty Fellowship (Award number N000142512047) and AFOSR FA9550-21-1-0177. T.C. acknowledges the support by the U.S. Department of Energy, Office of Basic Energy Sciences, under Contract No. DE-SC0025327. T.C. and D.X. acknowledge the support by the Computational Materials Sciences Program funded by the U.S. Department of Energy, Office of Science, Basic Energy Sciences, Materials Sciences, and Engineering Division, PNNL FWP 83557. L.J. acknowledges the support from the U.S. DOE, BES, under the award DE-SC0025325, the MIT-Portugal Program Seed Fund and NSF grant DMR-2414725. L.F. acknowledges the support from the Air Force Office of Scientific Research (AFOSR) under Award No.FA9550-22-1-0432 and the Simons Foundation. L.F. acknowledges the MIT SuperCloud and Lincoln Laboratory Supercomputing Center for providing computing resources.

LITERATURE CITED

1. Klitzing Kv, Dorda G, Pepper M. 1980. *Phys. Rev. Lett.* 45(6):494–497
2. Tsui DC, Stormer HL, Gossard AC. 1982. *Phys. Rev. Lett.* 48(22):1559–1562
3. Laughlin RB. 1983. *Phys. Rev. Lett.* 50(18):1395–1398
4. Kitaev A. 2003. *Annals of Physics* 303(1):2–30
5. Halperin BI. 1984. *Phys. Rev. Lett.* 52(18):1583–1586
6. Arovas D, Schrieffer JR, Wilczek F. 1984. *Phys. Rev. Lett.* 53(7):722–723
7. Moore G, Read N. 1991. *Nuclear Physics B* 360(2):362–396
8. Wen XG. 1991. *Phys. Rev. Lett.* 66(6):802–805
9. Nayak C, Simon SH, Stern A, Freedman M, Das Sarma S. 2008. *Rev. Mod. Phys.* 80(3):1083–1159
10. Stern A, Lindner NH. 2013. *Science* 339(6124):1179–1184
11. Lindner NH, Berg E, Refael G, Stern A. 2012. *Phys. Rev. X* 2(4):041002
12. Vaezi A, Barkeshli M. 2014. *Phys. Rev. Lett.* 113(23):236804
13. Das Sarma S, Freedman M, Nayak C. 2005. *Phys. Rev. Lett.* 94(16):166802
14. de Picciotto R, Reznikov M, Heiblum M, Umansky V, Bunin G, Mahalu D. 1997. *Nature* 389:162
15. M. Dolev M. Heiblum VUASDM. 2008. *Nature* 452:829

16. Alicea J, Fendley P. 2016. *Annual Review of Condensed Matter Physics* 7(Volume 7, 2016):119–139
17. Bartolomei H, Kumar M, Bisognin R, Marguerite A, Berroir JM, et al. 2020. *Science* 368(6487):173–177
18. Nakamura J, Liang S, Gardner GC, Manfra MJ. 2020. *Nature Physics* 16(9):931
19. Thouless DJ, Kohmoto M, Nightingale MP, den Nijs M. 1982. *Phys. Rev. Lett.* 49(6):405–408
20. Niu Q, Thouless DJ, Wu YS. 1985. *Phys. Rev. B* 31(6):3372–3377
21. Haldane FDM. 1988. *Phys. Rev. Lett.* 61(18):2015–2018
22. Kane CL, Mele EJ. 2005. *Phys. Rev. Lett.* 95(22):226801
23. König M, Wiedmann S, Brüne C, Roth A, Buhmann H, et al. 2007. *Science* 318(5851):766–770
24. Bernevig BA, Hughes TL, Zhang SC. 2006. *Science* 314(5806):1757–1761
25. Fu L, Kane CL. 2007. *Phys. Rev. B* 76(4):045302
26. Yu R, Zhang W, Zhang HJ, Zhang SC, Dai X, Fang Z. 2010. *Science* 329(5987):61–64
27. Chang CZ, Zhang J, Feng X, Shen J, Zhang Z, et al. 2013. *Science* 340(6129):167–170
28. Halperin BI, Jain JK. 2020. *World Scientific*
29. Kalmeyer V, Laughlin RB. 1989. *Phys. Rev. B* 39(16):11879–11899
30. Kol A, Read N. 1993. *Phys. Rev. B* 48(12):8890–8898
31. Hafezi M, Sørensen AS, Demler E, Lukin MD. 2007. *Phys. Rev. A* 76(2):023613
32. Sørensen AS, Demler E, Lukin MD. 2005. *Phys. Rev. Lett.* 94(8):086803
33. Palmer RN, Jaksch D. 2006. *Phys. Rev. Lett.* 96(18):180407
34. Möller G, Cooper NR. 2009. *Phys. Rev. Lett.* 103(10):105303
35. Kapit E, Mueller E. 2010. *Phys. Rev. Lett.* 105(21):215303
36. Sun K, Gu Z, Katsura H, Das Sarma S. 2011. *Phys. Rev. Lett.* 106(23):236803
37. Tang E, Mei JW, Wen XG. 2011. *Phys. Rev. Lett.* 106(23):236802
38. Neupert T, Santos L, Chamon C, Mudry C. 2011. *Phys. Rev. Lett.* 106(23):236804
39. D.N. Sheng Zheng-Cheng Gu KSLS. 2011. *Nature Communications* 2(389)
40. Regnault N, Bernevig BA. 2011. *Phys. Rev. X* 1(2):021014
41. Di Xiao Wenguang Zhu YRNNSO. 2011. *Nature Communications* 2(596)
42. Dean CR, Wang L, et al. 2013. *Nature* 497:598
43. Ponomarenko LA, Gorbachev RV, Yu GL, Elias DC, Jalil R, et al. 2013. *Nature* 497:594
44. Hunt B, Sanchez-Yamagishi JD, Young AF, Yankowitz M, LeRoy BJ, et al. 2013. *Science* 340(6139):1427–1430
45. Li G, Luican A, Lopes dos Santos JMB, Castro Neto AH, Reina A, et al. 2010. *Nature Physics* 6(6):109
46. Bistritzer R, MacDonald AH. 2011. *Proceedings of the National Academy of Sciences* 108(30):12233–12237
47. Yuan Cao Valla Fatemi ADSFSLTJYLJDSYKWTTEKRCAPJH. 2018. *Nature* 556:80
48. Yuan Cao Valla Fatemi SFKWTTEKPJH. 2018. *Nature* 556:43
49. Sharpe AL, Fox EJ, Barnard AW, Finney J, Watanabe K, et al. 2019. *Science* 365(6453):605–608
50. Serlin M, Tschirhart CL, Polshyn H, Zhang Y, Zhu J, et al. 2020. *Science* 367(6480):900–903
51. Spanton EM, Zibrov AA, Zhou H, Taniguchi T, Watanabe K, et al. 2018. *Science* 360(6384):62–66
52. Xie Y, Pierce AT, Park JM, Parker DE, Khalaf E, et al. 2021. *Nature* 600:439
53. Park H, Cai J, Anderson E, Zhang Y, Zhu J, et al. 2023. *Nature* 622:74
54. Lu Z, Han T, Yao Y, Reddy AP, Yang J, et al. 2024. *Nature* 626(8000):759–764
55. Wu F, Lovorn T, Tutuc E, Martin I, MacDonald AH. 2019. *Phys. Rev. Lett.* 122(8):086402
56. Yu H, Chen M, Yao W. 2019. *National Science Review* 7(1):12–20
57. Zhai D, Yao W. 2020. *Phys. Rev. Mater.* 4(9):094002
58. Liu K, Zhang L, Cao T, Jin C, Qiu D, et al. 2014. *Nature communications* 5(1):4966
59. He J, Hummer K, Franchini C. 2014. *Phys. Rev. B* 89(7):075409

60. Mak KF, Shan J. 2022. *Nature Nanotechnology* 17(7):686–695
61. Huang D, Choi J, Shih CK, Li X. 2022. *Nature nanotechnology* 17(3):227–238
62. Xiao D, Liu GB, Feng W, Xu X, Yao W. 2012. *Phys. Rev. Lett.* 108(19):196802
63. Cao T, Wang G, Han W, Ye H, Zhu C, et al. 2012. *Nat. Commun.* 3(1):887
64. Devakul T, Crepel V, Zhang Y, Fu L. 2021. *Nat Commun* 12:6730
65. Li H, Kumar U, Sun K, Lin SZ. 2021. *Phys. Rev. Res.* 3(3):L032070
66. Crépel V, Fu L. 2023. *Physical Review B* 107(20):L201109
67. Wu M, Li J. 2021. *Proceedings of the National Academy of Sciences* 118(50):e2115703118
68. Yasuda K, Wang X, Watanabe K, Taniguchi T, Jarillo-Herrero P. 2021. *Science* 372(6549):1458–1462
69. Enaldiev VV, Zólyomi V, Yelgel C, Magorrian SJ, Fal'ko VI. 2020. *Phys. Rev. Lett.* 124(20):206101
70. Magorrian SJ, Enaldiev VV, Zólyomi V, Ferreira F, Fal'ko VI, Ruiz-Tijerina DA. 2021. *Phys. Rev. B* 104(12):125440
71. Zhang X, Wang C, Liu X, Fan Y, Cao T, Xiao X. 2024. *Nature Communications* 15:4223
72. Cai J, Anderson E, Wang C, Zhang X, Liu X, et al. 2023. *Nature* 622:63
73. Zeng Y, Xia Z, Kang K, Zhu J, Knüppel P, et al. 2023. *Nature* 622:69
74. Foutty BA, Kometter CR, Devakul T, Reddy AP, Watanabe K, et al. 2024. *Science* 384(6693):343–347
75. Jia Y, Yu J, Liu J, Herzog-Arbeitman J, Qi Z, et al. 2024. *Phys. Rev. B* 109(20):205121
76. Mao N, Xu C, Li J, Bao T, Liu P, et al. 2024. *Communications Physics* 7(1):262
77. Wang C, Zhang XW, Liu X, He Y, Xu X, et al. 2024. *Phys. Rev. Lett.* 132(3):036501
78. Reddy AP, Alsallom F, Zhang Y, Devakul T, Fu L. 2023. *Phys. Rev. B* 108(8):085117
79. Qiu WX, Li B, Luo XJ, Wu F. 2023. *Phys. Rev. X* 13(4):041026
80. Yu J, Herzog-Arbeitman J, Wang M, Vafek O, Bernevig BA, Regnault N. 2024. *Phys. Rev. B* 109(4):045147
81. Reddy AP, Fu L. 2023. *Phys. Rev. B* 108(24):245159
82. Abouelkomsan A, Reddy AP, Fu L, Bergholtz EJ. 2024. *Phys. Rev. B* 109(12):L121107
83. Morales-Durán N, Wei N, Shi J, MacDonald AH. 2024. *Phys. Rev. Lett.* 132(9):096602
84. Lu T, Santos LH. 2024. *Phys. Rev. Lett.* 133(18):186602
85. Dong J, Wang J, Ledwith PJ, Vishwanath A, Parker DE. 2023. *Phys. Rev. Lett.* 131(13):136502
86. Goldman H, Reddy AP, Paul N, Fu L. 2023. *Phys. Rev. Lett.* 131(13):136501
87. Stern A, Fu L. 2024. *Phys. Rev. Lett.* 133(24):246602
88. Reddy AP, Paul N, Abouelkomsan A, Fu L. 2024. *Phys. Rev. Lett.* 133(16):166503
89. Wang C, Zhang XW, Liu X, Wang J, Cao T, Xiao D. 2025. *Phys. Rev. Lett.* 134(7):076503
90. Xu C, Mao N, Zeng T, Zhang Y. 2025. *Phys. Rev. Lett.* 134(6):066601
91. Ahn CE, Lee W, Yananose K, Kim Y, Cho GY. 2024. *Phys. Rev. B* 110(16):L161109
92. Chen F, Luo WW, Zhu W, Sheng DN. 2025. *Nature Communications* 16:2115
93. Anderson E, Fan FR, Cai J, Holtzmann W, Taniguchi T, et al. 2023. *Science* 381(6655):325–330
94. Park H, Cai J, Anderson E, Zhang X, Liu X, et al. 2025. *Nature Physics*
95. Xu X. 2024. *KITP Conference: Moiré materials: A New Paradigm in Tunable Quantum Matter, https://online.kitp.ucsb.edu/online/moire-c24/xu/*
96. Kang K, Qiu Y, Shen B, Lee K, Xia Z, et al. 2025. *arXiv*
97. Lezama IG, Arora A, Ubaldini A, Barreteau C, Giannini E, et al. 2015. *Nano Letters* 15:2336
98. Robert C, Picard R, Lagarde D, Wang G, Echeverry JP, et al. 2016. *Phys. Rev. B* 94(15):155425
99. Wang L, Shih EM, Ghiotto A, Xian L, Rhodes DA, et al. 2020. *Nature* 19:861
100. Ghiotto A, Shih EM, Pereira GSSG, Rhodes DA, Kim B, et al. 2021. *Nature* 597:345
101. Xu F, Sun Z, Jia T, Liu C, Xu C, et al. 2023. *Phys. Rev. X* 13(3):031037
102. Park H, Li W, Hu C, Beach C, Gonçalves M, et al. 2025.

https://www.arxiv.org/abs/2503.10989
103. Fan Xu Zheng Sun JLCZCXJGTJKWTTBTLLJJZSSJYZYZSLXLTL. 2025. *arXiv:2504.06972*
104. Aronson SH, Han T, Lu Z, Yao Y, Watanabe K, et al. 2024. *arXiv preprint arXiv:2408.11220*
105. Ji Z, Park H, Barber ME, Hu C, Watanabe K, et al. 2024. *Nature* 635:578
106. Redekop E, Zhang C, Park H, Cai J, Anderson E, et al. 2024. *Nature* 635:584
107. Anderson E, Cai J, Reddy AP, Park H, Holtzmann W, et al. 2024. *Nature* 635:590
108. Willett R, Eisenstein JP, Störmer HL, Tsui DC, Gossard AC, English JH. 1987. *Phys. Rev. Lett.* 59(15):1776–1779
109. Jain JK. 1989. *Phys. Rev. Lett.* 63(2):199–202
110. Halperin BI, Lee PA, Read N. 1993. *Phys. Rev. B* 47(12):7312–7343
111. Willett RL, Ruel RR, West KW, Pfeiffer LN. 1993. *Phys. Rev. Lett.* 71(23):3846–3849
112. Kang W, Stormer HL, Pfeiffer LN, Baldwin KW, West KW. 1993. *Phys. Rev. Lett.* 71(23):3850–3853
113. Goldman VJ, Su B, Jain JK. 1994. *Phys. Rev. Lett.* 72(13):2065–2068
114. Eisenstein JP, Pfeiffer LN, West KW. 1992. *Phys. Rev. Lett.* 69(26):3804–3807
115. Moore G, Read N. 1991. *Nuclear Physics B* 360(2-3):362–396
116. Read N. 2001. *Physica B: Condensed Matter* 298(1):121–128International Conference on High Magnetic Fields in Semiconductors
117. Read N, Green D. 2000. *Phys. Rev. B* 61(15):10267–10297
118. Morf RH. 1998. *Phys. Rev. Lett.* 80(7):1505–1508
119. Mitali Banerjee Moty Heiblum VUDEFYOAS. 2018. *Nature* 559:205
120. Zhang YH. 2024. *Phys. Rev. B* 110(15):155102
121. Xu Fan CX, Xiao J, Zhang Y, Liu F, Sun Z, et al. 2025. *Nature Physics*
122. Kang K, Shen B, Qiu Y, Zeng Y, Xia Z, et al. 2024. *Nature* 628:522
123. Sodemann Villadiego I. 2024. *Phys. Rev. B* 110(4):045114
124. Shi Y, Kahn J, Niu B, Fei Z, Sun B, et al. 2019. *Science Advances* 5(2):eaat8799
125. Lipson HS, Stokes A. 1942. *Proceedings of the Royal Society of London. Series A. Mathematical and Physical Sciences* 181(984):101–105
126. Wilhelm H, Croset B, Medjahdi G. 2007. *Carbon* 45(12):2356–2364
127. Lui CH, Li Z, Chen Z, Klimov PV, Brus LE, Heinz TF. 2011. *Nano letters* 11(1):164–169
128. Min H, MacDonald AH. 2008. *Progress of Theoretical Physics Supplement* 176:227–252
129. Zhang F, Sahu B, Min H, MacDonald AH. 2010. *Physical Review B—Condensed Matter and Materials Physics* 82(3):035409
130. Koshino M, McCann E. 2009. *Physical Review B—Condensed Matter and Materials Physics* 80(16):165409
131. Zhang F, Jung J, Fiete GA, Niu Q, MacDonald AH. 2011. *Physical review letters* 106(15):156801
132. Lui CH, Li Z, Mak KF, Cappelluti E, Heinz TF. 2011. *Nature Physics* 7(12):944–947
133. Bao W, Jing L, Velasco Jr J, Lee Y, Liu G, et al. 2011. *Nature Physics* 7(12):948–952
134. Zhang L, Zhang Y, Camacho J, Khodas M, Zaliznyak I. 2011. *Nature Physics* 7(12):953–957
135. Zou K, Zhang F, Clapp C, MacDonald A, Zhu J. 2013. *Nano letters* 13(2):369–373
136. Heeger AJ, Kivelson S, Schrieffer JR, Su WP. 1988. *Reviews of Modern Physics* 60(3):781
137. Velasco Jr J, Jing L, Bao W, Lee Y, Kratz P, et al. 2012. *Nature nanotechnology* 7(3):156–160
138. Lee Y, Tran D, Myhro K, Velasco J, Gillgren N, et al. 2014. *Nature communications* 5(1):5656
139. Myhro K, Che S, Shi Y, Lee Y, Thilahar K, et al. 2018. *2D Materials* 5(4):045013
140. Weitz RT, Allen MT, Feldman BE, Martin J, Yacoby A. 2010. *Science* 330(6005):812–816
141. Geisenhof FR, Winterer F, Seiler AM, Lenz J, Xu T, et al. 2021. *Nature* 598(7879):53–58
142. Han T, Lu Z, Scuri G, Sung J, Wang J, et al. 2024. *Nature Nanotechnology* 19(2):181–187
143. Liu K, Zheng J, Sha Y, Lyu B, Li F, et al. 2024. *Nature nanotechnology* 19(2):188–195
144. Shi Y, Xu S, Yang Y, Slizovskiy S, Morozov SV, et al. 2020. *Nature* 584(7820):210–214

145. Zhang Y, Tang TT, Girit C, Hao Z, Martin MC, et al. 2009. *Nature* 459(7248):820–823
146. Ju L, Shi Z, Nair N, Lv Y, Jin C, et al. 2015. *Nature* 520(7549):650–655
147. Ju L, Wang L, Cao T, Taniguchi T, Watanabe K, et al. 2017. *Science* 358(6365):907–910
148. Yang J, Chen G, Han T, Zhang Q, Zhang YH, et al. 2022. *Science* 375(6586):1295–1299
149. Han T, Lu Z, Yao Y, Yang J, Seo J, et al. 2024. *Science* 384(6696):647–651
150. Xiao D, Yao W, Niu Q. 2007. *Physical review letters* 99(23):236809
151. Han T, Lu Z, Scuri G, Sung J, Wang J, et al. 2023. *Nature* 623(7985):41–47
152. Zhou H, Xie T, Ghazaryan A, Holder T, Ehrets JR, et al. 2021. *Nature* 598(7881):429–433
153. Xue J, Sanchez-Yamagishi J, Bulmash D, Jacquod P, Deshpande A, et al. 2011. *Nature materials* 10(4):282–285
154. Decker R, Wang Y, Brar VW, Regan W, Tsai HZ, et al. 2011. *Nano letters* 11(6):2291–2295
155. Yankowitz M, Xue J, Cormode D, Sanchez-Yamagishi JD, Watanabe K, et al. 2012. *Nature physics* 8(5):382–386
156. Chen G, Jiang L, Wu S, Lyu B, Li H, et al. 2019. *Nature Physics* 15(3):237–241
157. Zhang YH, Mao D, Cao Y, Jarillo-Herrero P, Senthil T. 2019. *Physical Review B* 99(7):075127
158. Chen G, Sharpe AL, Fox EJ, Zhang YH, Wang S, et al. 2020. *Nature* 579(7797):56–61
159. Sha Y, Zheng J, Liu K, Du H, Watanabe K, et al. 2024. *Science* 384(6694):414–419
160. Choi Y, Choi Y, Valentini M, Patterson CL, Holleis LF, et al. 2025. *Nature* :1–6
161. Deng Y, Yu Y, Shi MZ, Guo Z, Xu Z, et al. 2020. *Science* 367(6480):895–900
162. Li T, Jiang S, Shen B, Zhang Y, Li L, et al. 2021. *Nature* 600(7890):641–646
163. Park Y, Kim Y, Chittari BL, Jung J. 2023. *Physical Review B* 108(15):155406
164. Lu Z, Han T, Yao Y, Hadjri Z, Yang J, et al. 2025. *Nature* :1–6
165. Xie J, Huo Z, Lu X, Feng Z, Zhang Z, et al. 2024. *Preprint at https://arxiv.org/abs/2405.16944*
166. Xia J, Pan W, Vicente C, Adams E, Sullivan N, et al. 2004. *Physical review letters* 93(17):176809
167. Liu Y, Pappas C, Shayegan M, Pfeiffer L, West K, Baldwin K. 2012. *Physical Review Letters* 109(3):036801
168. Eisenstein J, Cooper K, Pfeiffer L, West K. 2002. *Physical Review Letters* 88(7):076801
169. Deng N, Kumar A, Manfra MJ, Pfeiffer L, West K, Csathy GA. 2012. *Physical review letters* 108(8):086803
170. Chen S, Ribeiro-Palau R, Yang K, Watanabe K, Taniguchi T, et al. 2019. *Physical review letters* 122(2):026802
171. Kumar A, Csáthy G, Manfra M, Pfeiffer L, West K. 2010. *Physical review letters* 105(24):246808
172. Seiler AM, Geisenhof FR, Winterer F, Watanabe K, Taniguchi T, et al. 2022. *Nature* 608(7922):298–302
173. Dong J, Wang T, Wang T, Soejima T, Zaletel MP, et al. 2024. *Physical Review Letters* 133(20):206503
174. Zhou B, Yang H, Zhang YH. 2024. *Physical Review Letters* 133(20):206504
175. Zeng Y, Guerci D, Crépel V, Millis AJ, Cano J. 2024. *Physical Review Letters* 132(23):236601
176. Soejima T, Dong J, Wang T, Wang T, Zaletel MP, et al. 2024. *Physical Review B* 110(20):205124
177. Dong Z, Patri AS, Senthil T. 2024. *Physical Review B* 110(20):205130
178. Tan T, Devakul T. 2024. *Physical Review X* 14(4):041040
179. Sheng D, Reddy AP, Abouelkomsan A, Bergholtz EJ, Fu L. 2024. *Physical Review Letters* 133(6):066601
180. Han T, Lu Z, Hadjri Z, Shi L, Wu Z, et al. 2024. *arXiv:2408.15233*
181. Clarke DJ, Alicea J, Shtengel K. 2013. *Nature communications* 4(1):1348
182. Lindner NH, Berg E, Refael G, Stern A. 2012. *Physical Review X* 2(4):041002
183. Vishwanath A. 2023. *J. Club Condens. Matter Phys*

184. Parameswaran S. 2024. *J. Club Condens. Matter Phys*
185. Kwan YH, Yu J, Herzog-Arbeitman J, Efetov DK, Regnault N, Bernevig BA. 2023. *arXiv preprint arXiv:2312.11617*
186. Yu J, Herzog-Arbeitman J, Kwan YH, Regnault N, Bernevig BA. 2024. *arXiv preprint arXiv:2407.13770*
187. Guo Z, Lu X, Xie B, Liu J. 2024. *Physical Review B* 110(7):075109
188. Kudo K, Nakai R, Nomura K. 2024. *Physical Review B* 110(24):245135
189. Xie M, Das Sarma S. 2024. *Physical Review B* 109(24):L241115
190. Dong Z, Patri AS, Senthil T. 2024. *Physical Review Letters* 133(20):206502
191. Huang K, Li X, Das Sarma S, Zhang F. 2024. *Physical Review B* 110(11):115146
192. Huang K, Das Sarma S, Li X. 2025. *Physical Review B* 111(7):075130
193. Tan T, May-Mann J, Devakul T. 2024. *arXiv preprint arXiv:2409.06775*
194. Das Sarma S, Xie M. 2024. *Physical Review B* 110(15):155148
195. Lu Z, Han T, Yao Y, Yang J, Seo J, et al. 2024. *arXiv preprint arXiv:2408.10203*
196. Han T, Lu Z, Hadjri Z, Shi L, Wu Z, et al. 2024. *arXiv:2408.15233*
197. Anderson E, Park H, Yang K, Cai J, Taniguchi T, et al. 2025. *arXiv:2503.02810*